INL/JOU-21-64698-Revision-0

Unlocking Failure Mechanisms and Improvement of Practical LiS Pouch Cells through In Operando Pressure Study

December 2021

Bin Li, Lu Cai, Nikolaus Cordes, Sangwook Kim, Corey Michael Efaw, Daniel J Murray, Eric J Dufek, Leidong Xu, Parameswara R. Chinnam, Hongyi Xu

Changing the World's Energy Future

Idaho National Laboratory

INL is a U.S. Department of Energy National Laboratory operated by Battelle Energy Alliance, LLC

INL/JOU-21-64698-Revision-0

Unlocking Failure Mechanisms and Improvement of Practical LiS Pouch Cells through In Operando Pressure Study

Bin Li, Lu Cai, Nikolaus Cordes, Sangwook Kim, Corey Michael Efaw, Daniel J Murray, Eric J Dufek, Leidong Xu, Parameswara R. Chinnam, Hongyi Xu

December 2021

Idaho National Laboratory
Idaho Falls, Idaho 83415

http://www.inl.gov

Prepared for the
U.S. Department of Energy
Under DOE Idaho Operations Office
Contract DE-AC07-05ID14517

Unlocking Failure Mechanisms and Improvement of Practical Li-S Pouch Cells Through in Operando Pressure Study

*Parameswara R. Chinnam[1], Leidong Xu[2], Lu Cai[3], Nikolaus L. Cordes[4], Sangwook Kim[1], Corey M. Efaw[1], Daniel J. Murray[5], Eric J. Dufek[1], Hongyi Xu[2] and Bin Li[1]**

[1]Energy Storage & Advanced Transportation Department, Idaho National Laboratory, Idaho Falls, ID 83415 US

[2]Mechanical Engineering, University of Connecticut, Storrs, CT 06269 US

[3]Materials Science and Engineering Department, Idaho National Laboratory, Idaho Falls, ID 83415 US

[4]Advanced Post Irradiation Examination Department, Idaho National Laboratory, Idaho Falls, ID 83415 US

[5]Advanced Characterization Department, Idaho National Laboratory, Idaho Falls, ID 83415 US

*E-mail: bin.li@inl.gov

Abstract

For Lithium-sulfur (Li-S) battery commercialization, the study at a pouch cell level is essential, as some problems ignored or deemed minimal at the smaller level could have a greater effect on the performance of the larger pouch cell. Herein, the failure mechanisms of Li-S pouch cells are deeply investigated via in operando pressure analysis. It is found that highly porous structures of cathodes/separators and slow electrolyte diffusion through cathodes/separators can both lead to poor initial wetting. Additionally, Li-metal anode dominates the thickness variation of the whole pouch cell, which is verified by in situ measured pressure variation. Consequently, a real-time approach that combined normalized pressure with dP/dV analysis is proposed and validated to diagnose the morphology evolution of Li-metal anode. Moreover, applied pressure and porosity/tortuosity ratio of the cathode are both identified as independent factors that influence anode performance. In addition to stabilizing anodes, high pressure is proven to improve the cathode connectivity and avoid cathode cracking over cycling, which improves the possibility of developing cathodes with high sulfur mass loading. This work provides insights into Li-S pouch cell design (e.g., cathode and separator) and highlights pathways to improve cell capacity and cycling performance with applied and monitored pressure.

Keywords: lithium-sulfur, pressure, failure mechanism, operando, pouch cell, wettability

1. Introduction

Lithium-sulfur (Li-S) batteries are recognized as one of the most promising energy storage technologies, due to the implementation of a low-cost sulfur cathode that is highly abundant in the earth crust and offers both high theoretical capacity (1672 $mAhg^{-1}$) and theoretical specific energy (~2600 Wh kg^{-1}).[1] However, it is extremely difficult to achieve the theoretical specific energy in practical application due to low utilization of intrinsic electrical and ionically insulating sulfur and discharged products (Li_2S_2/Li_2S)[2]. Moreover, Li-S batteries severely suffer from short lifespan caused by the shuttling effect due to the dissolution of intermediate polysulfides into the electrolyte[3], as well as significant degradation and huge volume expansion of both anode[4] and cathode[2, 5] during operation. So far, tremendous efforts have been made to address the above issues at materials level, such as the discovery of new electrolytes to suppress polysulfide dissolution[6], the development of host materials to constrain/absorb soluble polysulfides[7], and the design of advanced coating materials onto the separator[8] or Li-metal anode surfaces[4, 9] to simultaneously minimize the polysulfide shuttling effect and Li-metal anode decay.

Coin cells are commonly used in the early stage of Li-S battery material development. However, the pouch cell format, with low weight cell packaging, is highly desirable for maximizing energy density at the cell level for practical applications.[10] It has been widely found that the progress made at the materials level of coin cells cannot be easily repeated in the practical pouch cells.[11] Many pronounced problems are detected in pouch cells that result in earlier cell failure, suggesting there is still a significant gap between scientific findings from coin cell level experiments and actual improvements to the pouch cell level. Hence, the investigations with respect to failure identification or performance improvements at pouch cell level are imperative and should be intensified in order to bridge the fundamentals of Li–S chemistry to the hindrance on its practical applications. Since 2017, with growing attention paid to the application of Li-S batteries, several pioneer works regarding Li-S pouch cell studies have been done by several groups. For instance, Barchasz et al.[12] observed large heat flow along with voltage disturbances in the Li-S pouch cells, which is ignored in coin cells and might result in failure mechanisms distinct from coin cells. Zhang's group found that Li metal powdering from dead Li formation is more responsible for poor cycling performances of Li-S pouch cells than the polysulfide shuttling issue.[11b] Further work suggested that the

nonuniformity of sulfur and lithium upon cycling is probed as one of the origins for the rapid capacity fading in a Li–S pouch cell.[13] Liu's group further confirmed the nonuniform distribution of sulfur species after cycling by combined X-ray absorption spectroscopy (XAS) and X-ray fluorescence (XRF) spectroscopy analysis, and they suggested catastrophic failure of high-energy Li–S pouch cells within the first tens of cycles resulted from uneven sulfur/polysulfide reactions and electrolyte depletion, rather than sulfur dissolution.[14] However, Ge et al.[15] found the capacity loss after the first cycle is mainly attributed to the dissolved sulfur species in electrolyte via the evaluation of 400 $Whkg^{-1}$ Li-S pouch cell. Therefore, the failure mechanisms of Li-S pouch cell still need to be explored and clarified.

Furthermore, in addition to the noticeable difference in electrode size (1.27 cm^2 of coin cell vs. 24 cm^2 of pouch cell in our work), a much higher stack pressure (> 1Mpa) is usually inherent on the compressed coin cell. It was taken for granted that stack pressure was playing a critical role, leading to inconsistent performance between pouch cells and coin cells. Moreover, external stack pressure has been proven to effectively suppress metallic lithium dendrite growth, thereby retarding the exacerbating formation of consumed lithium (e.g., solid electrolyte interphase (SEI) and dead Li) and stabilizing Li-metal anode in other batteries (e.g. Li-metal-Ni-rich $LiNi_{1-y-z}Mn_yCo_zO_2$ (NMC) cells).[16] In addition, with increasing size of the cells (especially for multi-layer pouch cells), the electrolyte wettability needs to be taken seriously. Otherwise, ionic conduction pathways and utilization of sulfur active materials in the cathodes would be significantly affected.[17]

Hence, in this work, the role of stack pressure on the performance of Li-S pouch cells was revealed. Additionally, monitored in operando mechanical response from the cell helped identify the factors that influence cell wettability and Li-metal anode performance at the pouch cell level, and develop an effective approach to real-time diagnosis of anode morphology evolution over cycling in Li-S pouch cell.

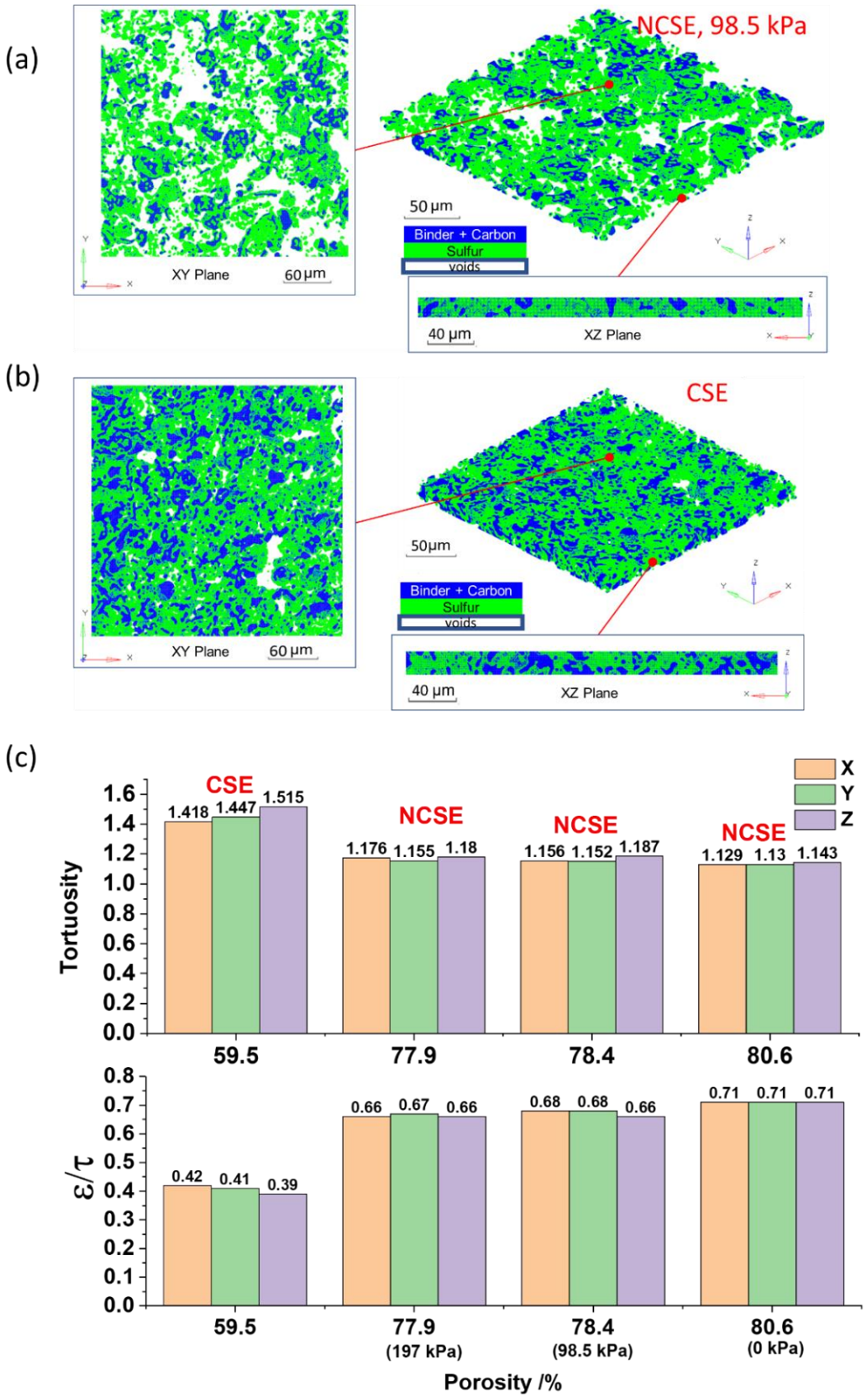

Figure 1. Micro-XCT images of 3D structures of NCSE under 98.5 kPa pressure(a) and CSE (b); (c) Tortuosity and ε/τ ratio of CSE and NCSE with different porosities and in different directions. (z direction: perpendicular to separators)

2. Results and Discussions

2.1. Sulfur Cathode Structures

It has been reported that both porosity[5, 17c, 18] and tortuosity[19] of cathodes can significantly affect the performance of Li-S coin cells. The high pressure applied onto Li-S pouch cell might alter the porosity and/or tortuosity of cathodes, which would interfere with the study on pressure effects. Consequently, two kinds of cathodes were prepared. One is non-calendared sulfur electrodes (NCSE) with a high porosity of 80.6%; the other is calendared sulfur electrode (CSE, with calendaring pressure > 1 Mpa) with a low porosity of 59.5%. As shown in **Figure S1**, ex situ stack pressures varying from 0 kPa to 400 kPa were applied onto both cathodes. NCSE underwent plastic deformation and gradual decrease in porosity from 80.6% to 72.0% along with a reduction in thickness. Alternatively, the porosity and thickness of CSE hardly changed, which was further examined by 2D cross-sectional X-radiographs of CSE via in situ stack pressures applied onto the CSE from 0 to 517 kPa. As shown in **Figure S2**, no obvious thickness change was observed between 0 and 517 kPa applied pressure, suggesting CSE would maintain a stable structure (i.e., constant porosity and tortuosity) and almost no elastic deformation would occur when under high pressure. These two sulfur cathodes provide preconditions to distinguish the effects of stack pressure and porosity/tortuosity on Li-S pouch cell performance.

In order to calculate the tortuosity of electrodes, the cathodes structures were characterized by micro-X-ray computed tomography (micro-XCT) using a laboratory-based X-ray microscope. **Figure 1** (a) and (b) shows typical micro-XCT images of NCSE (98.5 kPa pressure applied) and CSE, respectively. The 3D visualizations of NCSE microstructures under 0 and 197 kPa are also provided in **Figure S3**. Based on micro-XCT analysis, tortuosity of the cathode is evaluated with a microstructural-resolved modeling approach (**Figure S4**). Figure 1(c) illustrates the simulated tortuosity results of these sulfur electrodes. Tortuosity is known to be directional, and it can be seen from Figure 1(c) that the cathodes under different pressures are isotropic in terms of tortuosity. The tortuosity of NCSE slightly increases with decreasing porosity from 80.6% to 77.9%. However, comparing with NCSE without stack pressures applied, the tortuosity of CSE is greatly enhanced by 32.5% when the porosity is reduced to 59.5%.

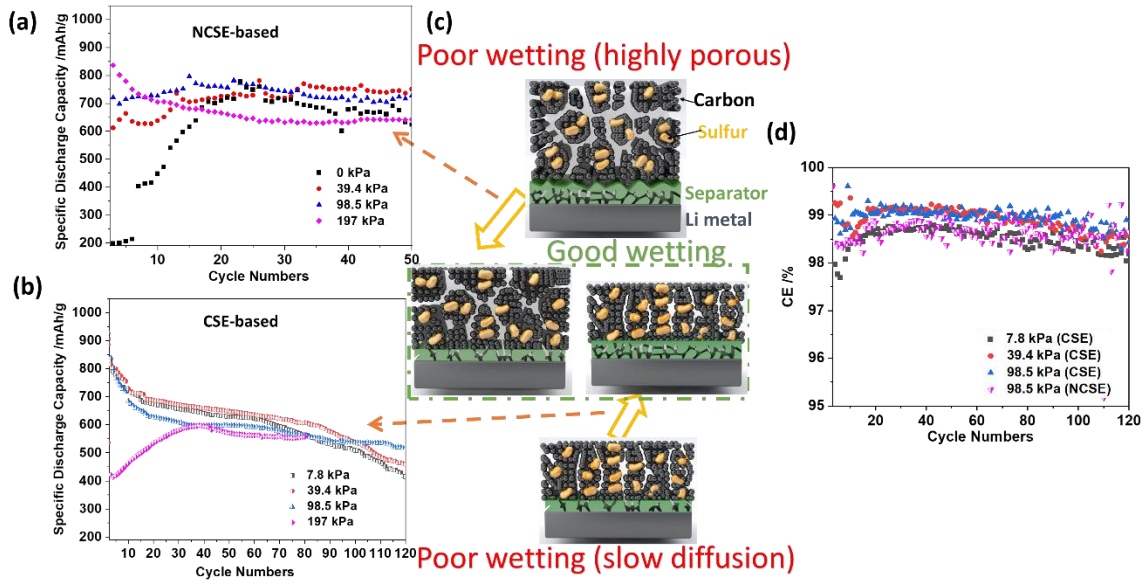

Figure 2. Specific discharge capacities of NCSE-based (a) and CSE-based (b) pouch cells over cycling as a function of stack pressures; (c) Schematic showing the mechanisms on poor wetting; (d) CE values over cycling as a function of pressures for different sulfur cathodes.

2.2. Wetting Issues

When increasing the cell size, new issues stand out, such as cell wettability, which is especially important for Li-S battery as it involves solid-liquid conversion during redox reaction.[17a] For both NCSE and CSE-based pouch cells, the cells rest for at least 8 hours before and after applying a certain pressure, ensuring sufficient time for electrolyte diffusion inside the electrodes/separator. However, for NCSE-based pouch cells, poor wetting occurs when pressure is excluded (in **Figure 2**(a) and **Figure S5**). When the stack pressure is increased from 0 to 197 kPa, the specific capacity over the first 15 cycles gradually increases, suggesting improved sulfur utilization driven by improved wettability. In contrast, as shown in Figure 2(b) and **Figure S6** (a), the wetting issue for CSE-based pouch cells under the low pressures is absent while present under the high pressure of 197 kPa over the first 30 cycles. It is therefore believed that the wetting mechanisms of the varied sulfur cathodes are different, as discussed below.

Carbon has been proven to possess poor electrolyte (1,3-dioxolane (DOL)/dimethoxyethane (DME)) wetting properties, which is attributed to lower binding energy between solvents and carbon, as reported in our previous work.[20] In a sulfur cathode, higher porosity corresponds to higher available carbon surface area. Schematically shown in Figure 2(c), the low

accessible capacity driven by poor wetting of the unpressurized NCSE cathode is ascribed to higher porosity (~ 80.6%) and inability of electrolyte to access active sulfur. With an increase in applied pressure to the NCSE-based pouch cell, the carbon nanoparticles (super P) are pressed more densely, resulting in reduced carbon surface areas. Therefore, accessible capacity increases due to a reduction in porosity that helps the electrolyte access more active sulfur material. The initial wetting issue occurring in the NCSE-based pouch cell under lower pressure is associated with higher cathode porosity. With increasing the cycles, the capacity gradually increases due to dissolution of polysulfides into the electrolytes, which helps to improve electrolyte wetting properties.[17c]

Notably, the high pressure will also compress the separator and close contact between electrodes and separator[21], which would slow electrolyte diffusion through the separator. Therefore, the poor wetting of CSE-based pouch cells only exists under a high pressure of 197 kPa, which correlates to the poor electrolyte diffusion driven by the compression of separators or reduced gaps between separators and electrodes rather than the cathodes in CSE-based pouch cells. This was further confirmed when the pressure was raised to 517 kPa, where the thickness of the cathode did not change (Figure S2). During operation of Li-S pouch cells, electrolyte depletion easily takes place near Li-metal anode where reaction with the electrolyte is preferential. When this occurs, the electrolyte needs to be replenished and diffuse from the edges of the pouch cells into the electrode bulk through the cathode or separator. Accordingly, the wetting issue present in the CSE-based pouch cell under high pressure is associated with slow electrolyte diffusion. When the pressure was reduced, the wetting was improved due to enhanced electrolyte diffusion through the separator. The larger the cell, the more important the electrolyte diffusion is for sulfur utilization. The wetting issue for CSEs was not observed in coin cells due to a much shorter electrolyte diffusion pathway from the edge of electrodes into the bulk of electrodes.[9b] Additionally, under the same pressure of 197 kPa, the CSE-based pouch cell is expected to possess the similar degree of separator compression/contact as the NCSE-based cell. However, the greatly enhanced wettability in NCSE-based cell (Figure 2(a) and (b)) suggests faster electrolyte diffusion through NCSE than CSE, which can be verified by quantifying diffusion capability in different cathode structures.

The relationship between electrode structures and liquid-phase diffusivity (of polysulfides in electrolyte in this case) inside the porous electrode can be described by following equation[22]:

$$D_{eff} = \frac{D_{int} \times \varepsilon}{\tau \times A} \qquad (1)$$

Here D_{eff} and D_{int} are the effective and intrinsic diffusion coefficients, respectively, of the liquid electrolyte through porous electrode. Porosity (ε), tortuosity (τ), and affinity (A, which is also philicity) are three parameters affecting the mass transport inside the porous electrode. According to Equation (1), for the fixed electrode materials and electrolytes, the effective diffusion coefficient for liquid transport through a porous structure is proportional to the ratio of ε/τ of such a porous structure. A higher ε/τ ratio represents faster liquid diffusion through the structure. As illustrated in Figure 1 (c), ε/τ ratio was reduced by 7.0% when the pressure was raised to 197 kPa for highly porous NCSE-based cells, suggesting the improved wettability under high pressure is due to the reduction in electrode and separator porosity rather than limitation of electrolyte diffusion. However, with the fixed pressure of 197 kPa, ε/τ ratio of CSE is only 58% of NCSE ε/τ ratio, corresponding to slower electrolyte diffusion through cathodes and poorer wettability of CSE when compared to NCSE. This suggests the wetting issue in the CSE-based pouch cell while under high pressure is mainly caused by slow electrolyte diffusion, which can be improved by optimizing both cathodes and separators.

By and large, in order to address the wetting issues in Li-S pouch cells, both the cathodes and separators should be considered with optimized porosity and ε/τ values in terms of electrolyte intake and diffusion. If high pressure is applied onto pouch cells, a robust separator with a stable structure in Li-S pouch cells is critically required, which was usually ignored in Li-S coin cell studies. Up to date, most studies on separators used in Li-S batteries have been focused on developing materials which could adsorb polysulfides to minimize the shuttling[8a, 23]. In addition to that, separators with optimized mass transportation characteristics and enhanced mechanical properties need to be taken seriously in the practical application of Li-S batteries.

2.3. Li-Metal Anode Evolution

For all the NCSE-based and CSE-based pouch cells, electrochemical and in operando pressure response was monitored as a function of applied pressure. The experimental setup is displayed in **Figure S7**. The representative plots of 98.5 kPa pressure overlaid with cycling voltage for CSE-based cell and NCSE-based cell are shown in **Figure 3**(a) and **Figure S8**, respectively. As shown in Figure S7, the pouch cell is inserted between two hard plates with a fixed gap. The gap can be adjusted according to the initial stack pressure set. During cell operation, shifts in pressure are mainly associated with the change in total thickness of the pouch cells.

For example, in Figure 3(a), during discharge, the decrease in pressure suggests the decreasing thickness of cell components. During discharge, lithium stripping occurs at the anode side, leading to a reduction in anode thickness; at the cathode side, elemental sulfur (S_8) converts to Li_2S through multiple polysulfide intermediate steps, which theoretically increases the volume of sulfur active materials by ~80%[2] and thus increases the thickness of the cathode. However, the pressure reduction was observed during discharge, implying the pressure variation is mainly dominated by the morphological changes of the anode. The anode's dominance in changing relative cell pressure is also true during charge. That agrees well with the previous finding on the cell thickness variation monitored by a laser gauge under operation.[24] Here, during discharge a slightly increased pressure is seen at the transition point between the upper and lower discharge plateau (clearly seen in 2nd discharge) that is associated with deposition of Li_2S solid precipitates on the cathode surface, leading to volumetric expansion. Nevertheless, the volume expansion at the cathode side is masked by Li stripping at the anode. The high porosity of cathodes can accommodate volume changes associated with sulfur during redox process, therefore reducing the pressure effect associated with sulfur volume changes, as confirmed in the voltage vs pressure response. That is indirectly confirmed by the voltage vs. pressure response of a pre-lithiated $Li_4Ti_5O_{12}$ (LTO)-S pouch cell (**Figure S9** (a) and (b)), in which pressure is nearly constant during charge/discharge, since LTO hardly undergoes volume change during cycling.[25]

As is mentioned above, Li-metal anode thickness evolution can be successfully echoed by the pressure variation. The factors to affect Li-metal anode thickness in Li-S pouch cells over cycling are investigated. The normalized pressure changes for Li-S pouch cells over cycling are shown in Figure 3(b) and (c). Normalized pressure changes were calculated by $P_{current}/P_{Initial}$ where $P_{Initial}$ and $P_{current}$ are initial setup pressure and real-time pressure over cycling, respectively. In Figure 3 (b), with a constant ε/τ value of CSE-based cathodes (0.39), the initial drop of normalized pressure, corresponding to the reduced anode thickness, is due to Li-metal loss caused by the generation/accumulation of polysulfides in the electrolytes. Afterwards, the normalized pressure keeps stable when higher external pressure is applied (39.4 kPa and 98.5 kPa), suggesting almost constant anode thickness and relatively stable anode structure in the later cycles. However, under low pressure of 7.8 kPa, a stable normalized pressure lasting a short time was followed by gradual increase in normalized pressure, suggesting increased anode thickness and unstable anode structure. Furthermore, when pressure is increased, the time required to stabilize normalized pressure, and therefore

anode structure, is decreased. As a result, the pressure has a positive effect on stabilizing Li-metal anode in Li-S pouch cells. High pressure could suppress the growth of high-surface area Li dendrites, thereby reducing formation of SEI/dead Li driven by side reaction between Li metal and electrolytes (polysulfides), leading to increased Columbic efficiency (CE) values in Figure 2(d) and specific capacity retention in Figure 2(b). Similarly, under the same pressure (98.5 kPa in Figure 3(c)), a smaller cathode ε/τ value, which represents slower electrolyte (polysulfide dissolved in the electrolyte) diffusion, is found to benefit Li-metal anode stabilization due to reduced side reaction on the anode surface. That is consistent with the increased CE values as ε/τ ratio decreases (Figure 2(d)).

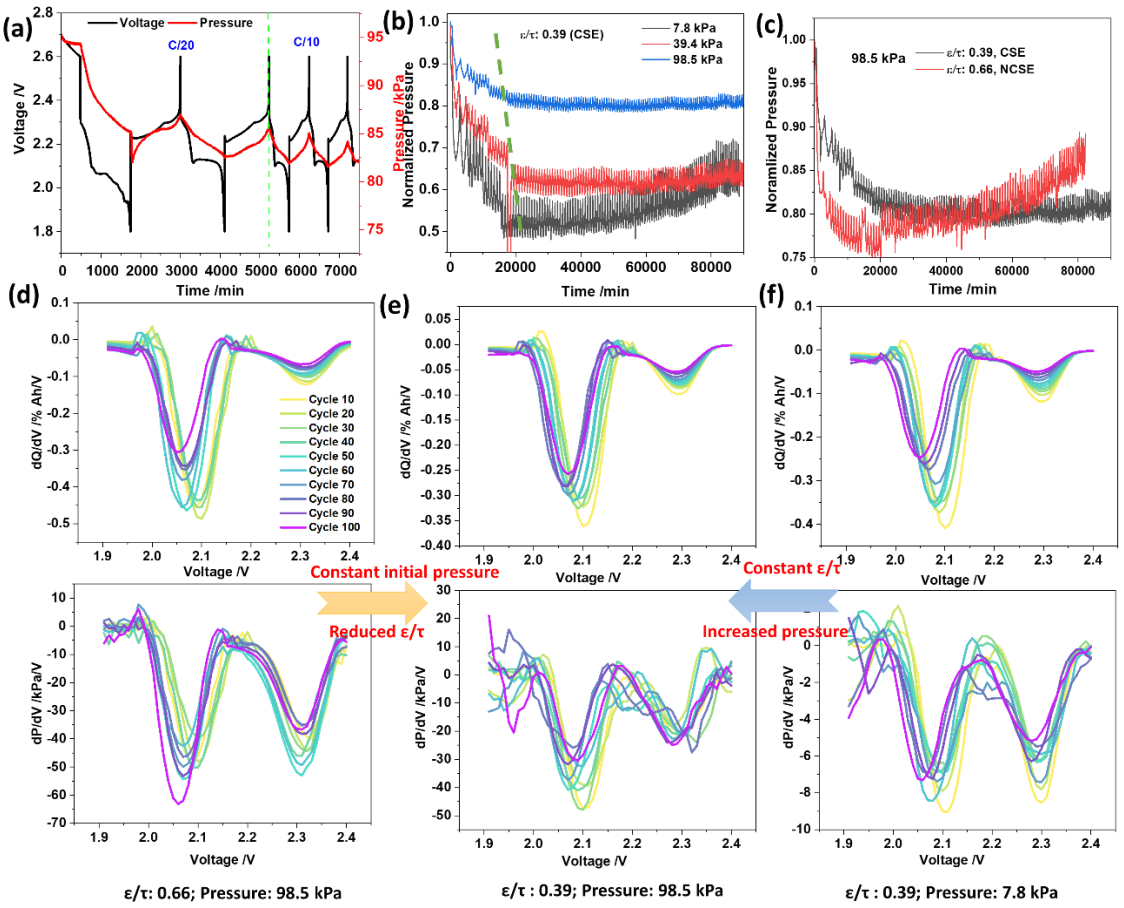

Figure 3. (a) The voltage and pressure variation during charge and discharge processes of CSE-based Li-S pouch cell under 98.5 kPa pressure; (b) Normalized pressure change trend for CSE-based pouch cells under different pressures with fixed ε/τ value of 0.39; (c) Normalized pressure change trend for the pouch cells with different ε/τ values under the same pressure of 98.5 kPa; dQ/dV and dP/dV curves over cycling during discharge process for NCSE-based cell (d) and CSE-based cell (e) under the pressure of 98.5 kPa as well as CSE-based cell under the pressure of 7.8 kPa (f).

Moreover, by comparing differential capacity (dQ/dV) with pressure (dP/dV) curves during discharge, the real-time Li-metal anode structure evolution can be inferred (Figure 3(d-f)). The dQ/dV peak intensity is proportional to the cell capacities. Supposing Li is stripped (at discharge) or plated (at charge) uniformly, the peak intensity of dP/dV over cycling is expected to follow the dQ/dV trend, which is found in the CSE-based pouch cell under 98.5 kPa pressure (Figure 3(e)). However, for highly porous NCSE-based cell under the same pressure of 98.5 kPa (Figure 3(d)), the peak intensity of dP/dV increases with decreasing peak intensities of dQ/dV starting from around 50 cycles, suggesting that high ε/τ value of the cathode could promote the formation of a porous anode structure caused by nonuniform Li stripping/plating, thus leading to significant anode thickness buildup (Figure 3(c)). Similarly, among CSE-based pouch cells with constant ε/τ value, we found peak intensity of dP/dV did not follow dQ/dV trend either in low-pressure cell (e.g. 7.8 kPa, Figure 3(f)), suggesting porous Li-metal anode structure is more easily generated under lower stack pressure. The proposed real-time diagnostic method for Li metal anode can also be used in other Li-metal batteries, such as Li-NMC battery.[26]

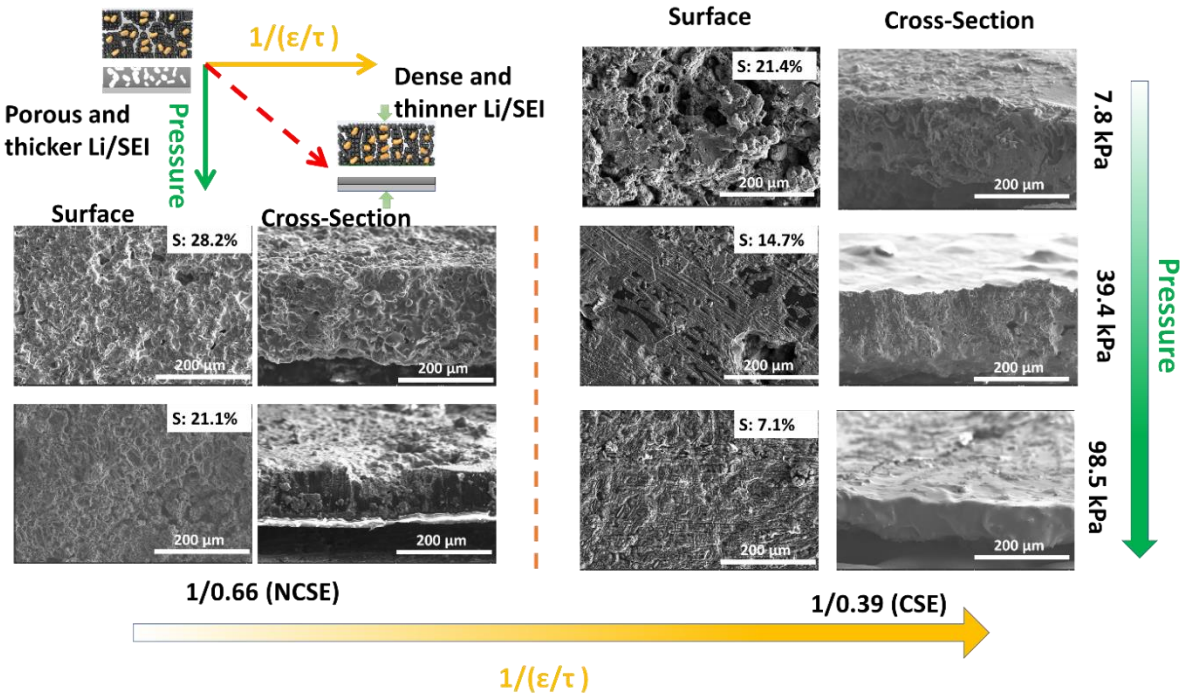

Figure 4. SEM images of Surface and cross-sectional morphologies of Li metal anodes in Li-S pouch cells at the end of charge after 120 cycles as a function of ε/τ values and stack pressures. The upper right corner of surface morphology images shows the mass fraction of sulfur near the surfaces.

In combination of the above analysis on normalized pressure and dP/dV (vs. dQ/dV), as schematically shown in **Figure 4** (upper left corner), higher τ/ε value of cathodes and external stack pressure onto Li-S pouch cells both should promote uniform Li stripping/plating, reduce side reaction, and suppress SEI/dead Li accumulation, thereby facilitating the denser and thinner anode structure over cycling. Those are validated with scanning electron microscopy (SEM) analysis of surfaces and cross-sectioned anode morphologies that were paired with cathodes of different ε/τ values as well as operated under different stack pressures, all analyzed after 120 cycles at the end of charge. The mass fraction of sulfur near Li metal anode surfaces obtained from elemental mapping with surface energy dispersive X-ray analysis (EDXA) is also displayed in Figure 4 (upper right corner of surface images). As seen in Figure 4, a smoother surface, denser and thinner cross-section, and lower sulfur content are observed in higher stack pressure and higher τ/ε (i.e., lower ε/τ) cells. As pressure or $1/(\varepsilon/\tau)$ decreases, mossy Li metal growth is observed, porous structure on the surfaces and cross-section is seen, as well as larger foil thickness and increased sulfur content on the surfaces. This post-mortem evidence agrees well with the inferences based on analysis from normalized pressure and dP/dV.

In summary, it was seen that an appropriately high stack pressure improves Li-S pouch cell cycling performance and safety (Figure 2(b) and Figure 4), while an inappropriately higher pressure causes wetting issues (Figure 2(b)). As is suggested above, in order for maximizing the role of the pressure, a robust separator needs to be explored, which is being studied. In addition, the combination of normalized pressure and dP/dV in operando monitoring design was verified as an effective tool for real-time diagnosis of Li-metal anode degradation (e.g., when significant degradation initiates; where the degradation is located by monitoring pressures at different locations across the large-scale cell) in Li-S pouch cells, which could be potentially incorporated into battery management system (BMS) design for practical Li-S batteries.

2.4. Pressure Effect on Sulfur Cathode

As is well known, the conversion between elemental sulfur (S_8) and Li_2S can experience a significant volume expansion of ~80% during cycling, which might inevitably lead to cracking and delamination from the current collector after extended cycling.[27] The generated cracks would result in sluggish Li^+/e^- transport and increased ε/τ values, thereby causing high cathode resistances (Figure S6(b)), low sulfur utilization, sulfur dissolution from the cathode,

as well as severe anode degradation. For addressing cathode fracture issue, one of the effective approaches studied by most groups is to develop flexible binders in cathodes.[28] Herein, we found the high pressure was also able to prevent cathode cracking. These cracks were seen on the surface of cathodes only in lower pressure pouch cell after 120 cycles (7.8 kPa, in **Figure 5**(b)). Moreover, the surface of cathodes became more porous when compared to fresh sulfur without cycling, due to severe solid sulfur loss over cycling. However, with increasing pressure (e.g., 98.5 kPa), the connection of cathode materials was improved, as verified by a reduced charge transfer resistance (**Figure S10**). For sulfur cathode under high pressure (98.5 kPa), no new generated cracks were observed on the surface after 120 cycles, while the surface morphology was similar to fresh sulfur cathode, suggesting that higher pressure could simultaneously prevent cracking and minimize shuttling. As studied above, pressure also has a positive effect on stabilizing the Li-metal anode. In order to further distinguish the role of pressure on sulfur cathode and Li-metal anode, a pre-lithiated LTO was used to replace Li-metal as the anode to study the function of stack pressure on the sulfur cathode (Figure S9). Comparing with the large volume expansion and poor cycle life of Li-metal, LTO used as an anode in other Li-ion batteries has been validated to be relatively stable[29]. Therefore, the influence of pressure on the LTO-S pouch cell should primarily stem from sulfur. In Figure S9 (c), the high pressure leads to an improved CE value, rising from 60% to 90%, which is due to the findings shown in Figure 5, confirming that high pressure can benefit the stabilization of the sulfur cathode in addition to the Li-metal anode.

Inspired by the above analysis, the poor connection of cathode materials and cracking over cycling, especially existing in high-S mass loading cathodes, would be effectively suppressed by applying relatively high pressure, which would benefit the weight reduction of conductive agents and binders used in the sulfur cathodes. Therefore, the application of pressure on practical sulfur cathodes is believed to stimulate the development of high-energy density Li-S batteries.

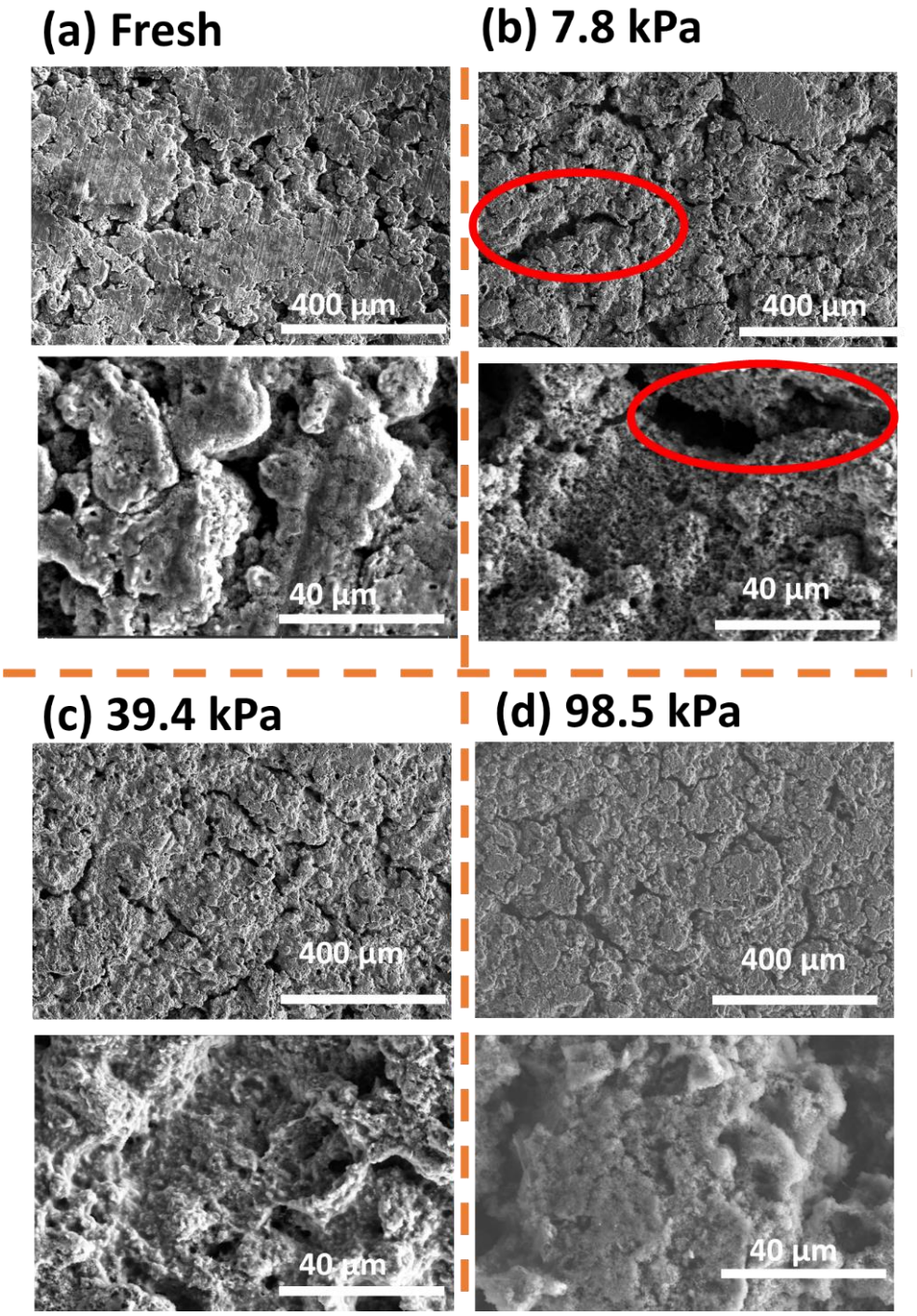

Figure 5. SEM images of Surface morphologies of sulfur electrodes in CSE-based pouch cells under the different pressures after 120 cycles at the end of charge. (a) fresh electrode without cycling; (b) 7.8 kPa; (c) 39.4 kPa; (d) 98.5 kPa.

3. Conclusion

In this work, the failure mechanisms of Li-S pouch cells were deeply understood, and the approaches to improve Li-S pouch cell performances were identified via in-situ monitoring of pressure applied onto pouch cells. First, the tortuosity (τ) values of kinds of cathodes (NCSEs

and CSE) were simulated with a microstructural-resolved modeling approach based on micro-XCT results. The initial wetting issue was identified to be caused by highly porous cathodes/separators and slow electrolyte diffusion through cathodes/separators. Hence, the porosity (ε) and ε/τ values of cathodes associated with electrolyte intake and diffusion, respectively, need to be optimized. A robust separator is highly required if high external pressure is used to improve Li-S pouch cell performances. Second, the thickness evolution of Li-S pouch cell reflected by cell pressure variation is mostly governed by Li metal anodes volume changes, which mask the response of the sulfur cathodes. The degradation of Li-metal anode can be diagnosed in real time by combing normalized pressure with dP/dV analysis, which is well validated with support from post-mortem analysis. Finally, external stack pressure is proven to help stabilize the Li-metal anode, as well as keep the sulfur cathode well connected and avoid cracking over cycling. In addition to high pressure, a small ε/τ ratio of the cathode structure was identified as another factor to promote uniform Li plating/stripping and suppress SEI/dead Li accumulation. We believe that the proposed work would shed light on Li-S pouch cell design, with primary focus on cathode and separator design, as well as the use of applying and monitoring pressure. The use of this pressure operating system for pouch cells would be of great help to improve cycling performance and increase energy density of Li-S batteries, as well as safely manage the pouch cell.

4. Experimental Section/Methods

4.1. Sulfur Cathode Preparation

The sulfur cathode was produced by mixing 1.28 g sulfur (Fisher Scientific, 99.5%) with 0.52 g super P (EQ-Lib-SuperP, MTI Corporation) conductive agent. This mixture was ball milled and further heat treated at 155°C in an autoclave. 0.2 g polyvinylidenefluoride (PVDF) binder mixed in 1-methyl-2-pyrrolidone (NMP, Sigma-Aldrich, ≥99%) solution is added to the S-C mix with an additional 5 g of NMP solvent, mixed with three 5 mm diameter zirconia balls in an ARE-310 Thinky Mixer for 5 minutes, resulting in 64% active mass. The slurry was rolled onto a 20 μm carbon-coated Al current collector (MTI Corporation) and dried in a furnace with dry air flow at 80°C for three days. The resultant electrode has ~3 $mgcm^{-2}$ of active sulfur weight with a porosity of ~80%. Some of the electrodes were further calendared to ~60% porosity. Both calendared and non-calendared sulfur electrodes were utilized in pouch cell preparation. The practical capacity for 1C of this sulfur is defined as 1000 $mAhg^{-1}$ (i.e., 3 $mAhcm^{-2}$).

4.2. Pouch Cell Preparation

Single layer pouch cells (43 mm × 56 mm) were assembled using a single-sided coated sulfur cathode (~ 3 $mAhcm^{-2}$) and lithium metal (50 μm of thickness, China Energy Lithium Co.) as the anode. Calendared cathodes and non-calendared cathodes were both used in the pouch cells. Celgard 2325 was used as a separator. The electrolytes of 1M lithium bis(trifluoromethanesulfonyl)imide (LiTFSI, BASF) and 2 wt.% of lithium nitrate ($LiNO_3$, Sigma-Aldrich) mixed in 1:1 DOL:DME (1,3-dioxolane (DOL, Sigma-Aldrich) and dimethoxyethane (DME, Sigma-Aldrich)) were prepared and used in each pouch cell with electrolyte-to-sulfur (E/S) ratio of 15 μL/mg. Single-layer pouch cells were also assembled with pre-lithiated $Li_4Ti_5O_{12}$ (LTO) and calendared sulfur cathode. For LTO-S pouch cells, active sulfur loading was adjusted to the capacity of pre-lithiated LTO electrodes.

4.3. Electrochemical Measurement

All pouch cells were cycled at 25 ± 1 °C inside a temperature-controlled environmental chamber (BTZ-133, ESPEC corp.) using a MACCOR Model 2200 (Maccor, Inc.). The Li-S pouch cells were cycled at the charge/discharge rate of C/10 (1C = 1000 mA g^{-1}) within the voltage range of 1.8-2.6 V versus Li/Li^+. All the cells rested for at least 8 hours at 25°C before and after applying pressures. Prior to cycling at C/10, two formation cycles at the charge/discharge rate of C/20 were performed. No rest time existed between charge and discharge procedures. LTO-S pouch cells were cycled between 0.05 and 1.0 V with two C/20 formation cycles followed by C/10 aging cycles. Electrochemical impedance spectroscopy (EIS) (Gamry potentiostat/galvanostat/ZRA (Interface 3000)) was used to analyze impedance spectra for pouch cells with applied perturbation voltage of 10 mV in the frequency range from 0.1Hz to 1 MHz.

4.4. Operando Pressure Measurement

Figure S7 shows the experimental setup to measure pressure evolution during cycling. The design uses a total of three G10 glass epoxy plates (Ridout Plastics Co. Inc.). The pouch cell was positioned between the first two plates, and 3 LCKD load cells (Omega Engineering Inc.) were placed between the middle and the last plates. In this study, different initial pressure conditions were imposed by adjusting the gap between the plates. This gap was fixed during cycling and the pressure evolution due to volume (thickness) changes in the cell were determined using the load cells. The experimental details can also be seen in our previous study.[26]

4.5. Post-Characterization

The surfaces and cross-sectional thickness/morphologies of cycled Li metal anode and sulfur electrodes were investigated with scanning electron microscopy (SEM) and elemental analysis (via energy dispersive X-ray spectroscopy, EDS) obtained with a FEI Teneo FESEM. The pouch cells were disassembled in an Ar-filled glove box, and electrodes used for post testing were dried inside the glove box in order for removing electrolyte solvent.

4.6. Micro X-ray Computed Tomography and in situ Compression/2D Radiography

Micro-XCT of NCSE and CSE was performed using a ZEISS Xradia 520 Versa X-ray microscope (Carl Zeiss X-ray Microscopy, Inc., Dublin, CA) operated using Scout-and-Scan Control System software (version 14.0.16046). The cone-beam, polychromatic X-ray source, which uses a tungsten target, was operated at 40 kVp peak accelerating voltage and 3 W. The X-ray beam was filtered using an LE2 filter and a 4X objective lens, coupled to a charge-coupled device (CCD) camera, and was used for optical magnification. For all the electrodes, 1601 radiographs were acquired over 360° sample rotation, with exposure times of 37 s (CSE) and 48.5 s (NCSE) and a camera binning of 2, resulting in FOVs of 1024 px × 1024 px. Sample/stage drift was corrected using the adaptive motion compensation option and ring artifact reduction was achieved using the dynamic ring removal option. Radiographs were reference-corrected by collecting 10 open-beam images at the beginning of data collection and again periodically through image acquisition. The resulting isotropic voxel edge length for each tomogram was within the range of 498-501 nm.

Reference-corrected radiographs were reconstructed into 3D tomograms using ZEISS Scout-and-Scan Control System Reconstructor software (version 14.0.160463.38913). The center shift for each tomogram was determined using the automated center shift feature. Beam hardening correction was performed using the software's Standard Beam Hardening Correction option at a beam hardening constant of 0.05. For all the electrodes, a smoothing filter with $\sigma = 0.05$ was applied. Reconstructed tomograms were processed using Thermo Scientific™ Avizo software (version 2020.3.1, Thermo Fisher Scientific, Waltham, MA) before image segmentation. Tomograms were aligned in the imaging plane using the translation tool to correct for sample tilt then resampled using the Resample module.

In situ compression testing of CSE was performed with a Deben CT5000-GCT-TEC load stage (Deben UK Ltd., London, England) equipped with a 540 N load cell and controlled using Deben Microtest software (v. 6.3.40). A polyoxymethylene right cylinder, 2 mm in height and 4.76 mm in diameter, was placed on the bottom stainless-steel platen of the load stage and was used to hold the electrode. A custom polycarbonate platen, with a diameter of 7 mm was used as the top platen. A 3.6 mm diameter CSE disc was inserted into two platens. 2D radiographs were acquired with a 40 kVp X-ray, 3W beam, 4X objective lens, and 30 s radiograph exposure with a camera binning of 2. The FOV of the radiographs was 1024 px × 1024 px with a 2D isotropic pixel size of 1.07 µm. The load stage was operated by moving the bottom platen towards the top platen to a specified force with a travel speed of 0.200 mm/min. Once the specified force was registered, movement was halted to acquire the radiograph. The maximum force applied was 517.1 kPa.

4.7. Tortuosity simulation

Tortuosity of the cathode is evaluated with a microstructural-resolved modeling approach (Figure S4). We established an image processing workflow to segment the 3D voxel tomographic image of the cathode microstructure. After denoising the 3D tomographic image, the voxels were classified into one of the three phases based on its greyscale value: sulfur, binder/carbon, and voids. The sulfur phases have higher greyscale values, while the pore phases have lower greyscale values. The percentage of voxels in each phase is equal to its volume fraction, which is calculated based on its weight fraction and density. Evaluation of tortuosity requires a binary voxel image matrix, where "1" represents the solid phase and "0" defines the pore network. The tortuosity factor of a pore network is simulated by comparing the steady-state diffusive flow through this network, $F_{network}$, to that through a fully dense control volume of the same dimension, diffusivity, and potential difference, $F_{control}$. Thus, the tortuosity factor τ is evaluated as:

$$\tau = \varepsilon \cdot \frac{F_{control}}{F_{network}} \quad (2)$$

where ε is the porosity of the microstructure. For a voxelated pore network, each cubic voxel is a basic element of the pore structure. The steady-state diffusion flow is simulated based on the concentration in each element only in terms of the concentrations of its face-adjacent neighbors. In this work, we applied the open-source MATLAB toolbox TauFactor[30] to solve the steady-state diffusion problem.

Supporting Information

Supporting Information is available from the Wiley Online Library or from the author.

Conflict of Interest

The authors declare no competing financial interest.

Acknowledgements

Research has been supported by the Assistant Secretary for Energy Efficiency and Renewable Energy, Office of Vehicle Technologies of the U.S. Department of Energy through the Advanced Battery Materials Research Program (Battery 500 Consortium). Idaho National Laboratory (INL) is operated by Battelle Energy Alliance under Contract Nos. DE-AC07-05ID14517 for the U.S. Department of Energy. The U.S. Government retains and the publisher, by accepting the article for publication, acknowledges that the United States Government retains a nonexclusive, paid-up, irrevocable, world-wide license to publish or reproduce the published form of this manuscript, or allow others to do so, for U.S. Government purposes. The work on tortuosity simulation by Prof. Hongyi Xu is supported by the start-up funding from the University of Connecticut. Dr. Bin Li would like to thank Dr. Jun Liu and Dr. Jie Xiao from Pacific Northwest National Laboratory for the meaningful discussions on this work and thank Charles C. Dickerson from Idaho National Laboratory for his help on pressure setup.

Received: ((will be filled in by the editorial staff))
Revised: ((will be filled in by the editorial staff))
Published online: ((will be filled in by the editorial staff))

References

[1] a) H. J. Peng, J. Q. Huang, X. B. Cheng, Q. Zhang, *Advanced Energy Materials* **2017**, 7, 1700260; b) M. Wild, L. O'neill, T. Zhang, R. Purkayastha, G. Minton, M. Marinescu, G. Offer, *Energy & Environmental Science* **2015**, 8, 3477; c) Q. Pang, X. Liang, C. Y. Kwok, L. F. Nazar, *Nature Energy* **2016**, 1, 1.

[2] P. Barai, A. Mistry, P. P. Mukherjee, *Extreme Mechanics Letters* **2016**, 9, 359.

[3] W. Ren, W. Ma, S. Zhang, B. Tang, *Energy Storage Materials* **2019**, 23, 707.

[4] H. Zhao, N. Deng, J. Yan, W. Kang, J. Ju, Y. Ruan, X. Wang, X. Zhuang, Q. Li, B. Cheng, *Chemical Engineering Journal* **2018**, 347, 343.

[5] G. He, S. Evers, X. Liang, M. Cuisinier, A. Garsuch, L. F. Nazar, *ACS nano* **2013**, 7, 10920.

[6] a) L. Wang, Y. Ye, N. Chen, Y. Huang, L. Li, F. Wu, R. Chen, *Advanced functional materials* **2018**, 28, 1800919; b) W. Chen, T. Lei, C. Wu, M. Deng, C. Gong, K. Hu, Y. Ma, L. Dai, W. Lv, W. He, *Advanced Energy Materials* **2018**, 8, 1702348.

[7] a) M. Zhang, W. Chen, L. Xue, Y. Jiao, T. Lei, J. Chu, J. Huang, C. Gong, C. Yan, Y. Yan, *Advanced Energy Materials* **2020**, 10, 1903008; b) D. McNulty, V. Landgraf, S. Trabesinger, *Journal of Materials Chemistry A* **2020**, 8, 26085.

[8] a) S. Bai, X. Liu, K. Zhu, S. Wu, H. Zhou, *Nature Energy* **2016**, 1, 1; b) J.-Q. Huang, Q. Zhang, F. Wei, *Energy Storage Materials* **2015**, 1, 127.

[9] a) G. Ma, Z. Wen, M. Wu, C. Shen, Q. Wang, J. Jin, X. Wu, *Chemical Communications* **2014**, 50, 14209; b) C. M. Efaw, B. Lu, Y. Lin, G. M. Pawar, P. R. Chinnam, M. F. Hurley, E. J. Dufek, Y. S. Meng, B. Li, *Materials Today* **2021**.

[10] S. Dörfler, H. Althues, P. Härtel, T. Abendroth, B. Schumm, S. Kaskel, *Joule* **2020**, 4, 539.

[11] a) T. Cleaver, P. Kovacik, M. Marinescu, T. Zhang, G. Offer, *Journal of The Electrochemical Society* **2017**, 165, A6029; b) X.-B. Cheng, C. Yan, J.-Q. Huang, P. Li, L. Zhu, L. Zhao, Y. Zhang, W. Zhu, S.-T. Yang, Q. Zhang, *Energy Storage Materials* **2017**, 6, 18.

[12] C. Barchasz, L. Boutafa, E. Mayousse, B. Chavillon, *Electrochimica Acta* **2018**, 292, 974.

[13] L. Kong, Q. Jin, J. Q. Huang, L. D. Zhao, P. Li, B. Q. Li, H. J. Peng, X. Zhang, Q. Zhang, *Energy Technology* **2019**, 7, 1900111.

[14] L. Shi, S.-M. Bak, Z. Shadike, C. Wang, C. Niu, P. Northrup, H. Lee, A. Y. Baranovskiy, C. S. Anderson, J. Qin, *Energy & Environmental Science* **2020**, 13, 3620.

[15] G. Ye, M. Zhao, L.-P. Hou, W.-J. Chen, X.-Q. Zhang, B.-Q. Li, J.-Q. Huang, *Journal of Energy Chemistry* **2022**, 66, 24.

[16] a) K. L. Harrison, S. Goriparti, L. C. Merrill, D. M. Long, B. Warren, S. A. Roberts, B. R. Perdue, Z. Casias, P. Cuillier, B. L. Boyce, *ACS Applied Materials & Interfaces* **2021**, 13, 31668; b) X. Zhang, Q. J. Wang, K. L. Harrison, K. Jungjohann, B. L. Boyce, S. A. Roberts, P. M. Attia, S. J. Harris, *Journal of The Electrochemical Society* **2019**, 166, A3639; c) C. Fang, B. Lu, G. Pawar, M. Zhang, D. Cheng, S. Chen, M. Ceja, J.-M. Doux, M. Cai, B. Liaw, *arXiv preprint arXiv:2008.07710* **2020**.

[17] a) D. Lv, J. Zheng, Q. Li, X. Xie, S. Ferrara, Z. Nie, L. B. Mehdi, N. D. Browning, J. G. Zhang, G. L. Graff, *Advanced Energy Materials* **2015**, 5, 1402290; b) J.-Y. Hwang, H. M. Kim, Y.-K. Sun, *Journal of The Electrochemical Society* **2017**, 165, A5006; c) D. Lu, Q. Li, J. Liu, J. Zheng, Y. Wang, S. Ferrara, J. Xiao, J.-G. Zhang, J. Liu, *ACS applied materials & interfaces* **2018**, 10, 23094.

[18] N. Kang, Y. Lin, L. Yang, D. Lu, J. Xiao, Y. Qi, M. Cai, *Nature communications* **2019**, 10, 1.

[19] a) H. Chen, G. Zhou, D. Boyle, J. Wan, H. Wang, D. Lin, D. Mackanic, Z. Zhang, S. C. Kim, H. R. Lee, *Matter* **2020**, 2, 1605; b) Y. Li, K. K. Fu, C. Chen, W. Luo, T. Gao, S. Xu, J. Dai, G. Pastel, Y. Wang, B. Liu, *ACS nano* **2017**, 11, 4801; c) J. Ma, Y. Qiao, M. Huang, H. Shang, H. Zhou, T. Li, W. Liu, M. Qu, H. Zhang, G. Peng, *Applied Surface Science* **2021**, 542, 148664.

[20] Y. Zhang, Y. Lin, L. He, V. Murugesan, G. Pawar, B. M. Sivakumar, H. Ding, D. Ding, B. Liaw, E. J. Dufek, *ACS Applied Energy Materials* **2020**, 3, 4173.

[21] S. Yan, *Characterization and Modelling of Polymeric Battery Separators for Crash Safety Simulation*, Michigan State University, **2019**.

[22] P. Grathwohl, *Diffusion in natural porous media: Contaminant transport, sorption/desorption and dissolution kinetics*, Springer Science & Business Media, **2012**.

[23] Z. A. Ghazi, X. He, A. M. Khattak, N. A. Khan, B. Liang, A. Iqbal, J. Wang, H. Sin, L. Li, Z. Tang, *Advanced Materials* **2017**, 29, 1606817.

[24] S. Waluś, G. Offer, I. Hunt, Y. Patel, T. Stockley, J. Williams, R. Purkayastha, *Energy Storage Materials* **2018**, 10, 233.

[25] T. Ohzuku, A. Ueda, N. Yamamoto, Y. Iwakoshi, *Journal of power sources* **1995**, 54, 99.

[26] S. Kim, A. Raj, B. Li, E. J. Dufek, C. C. Dickerson, H.-Y. Huang, B. Liaw, G. M. Pawar, *Journal of Power Sources* **2020**, 463, 228180.

[27] a) M. He, Y. Li, S. Liu, R. Guo, Y. Ma, J. Xie, H. Huo, X. Cheng, G. Yin, P. Zuo, *Chemical Communications* **2020**, 56, 10758; b) J. Liu, D. G. Galpaya, L. Yan, M. Sun, Z. Lin, C. Yan, C. Liang, S. Zhang, *Energy & Environmental Science* **2017**, 10, 750.

[28] a) H. Yuan, J. Q. Huang, H. J. Peng, M. M. Titirici, R. Xiang, R. Chen, Q. Liu, Q. Zhang, *Advanced Energy Materials* **2018**, 8, 1802107; b) Q. Qi, X. Lv, W. Lv, Q.-H. Yang, *Journal of Energy Chemistry* **2019**, 39, 88.

[29] T.-F. Yi, Y. Xie, Y.-R. Zhu, R.-S. Zhu, H. Shen, *Journal of Power Sources* **2013**, 222, 448.

[30] a) H. Xu, F. Usseglio-Viretta, S. Kench, S. J. Cooper, D. P. Finegan, *Journal of Power Sources* **2020**, 480, 229101; b) S. J. Cooper, A. Bertei, P. R. Shearing, J. Kilner, N. P. Brandon, *SoftwareX* **2016**, 5, 203; c) N. Hoffman, J. Lee, W. Li, J. Zhu, H. Xu, presented at ECS Meeting Abstracts **2021.**

Through operando pressure study on practical Li-S pouch cell, the pressure roles and the failure mechanisms on poor wetting are revealed, and the Li metal anode degradation can be diagnosed in real time. Those can shed light on the rational design of high-energy density Li-S battery and materials development at the pouch cell level.

Parameswara R. Chinnam[1], Leidong Xu[2], Lu Cai[3], Nikolaus L. Cordes[4], Sangwook Kim[1], Corey M. Efaw[1], Daniel J. Murray[5], Eric J. Dufek[1], Hongyi Xu[2] and Bin Li[1]*

Unlocking Failure Mechanisms and Improvement of Practical Li-S Pouch Cells Through in Operando Pressure Study

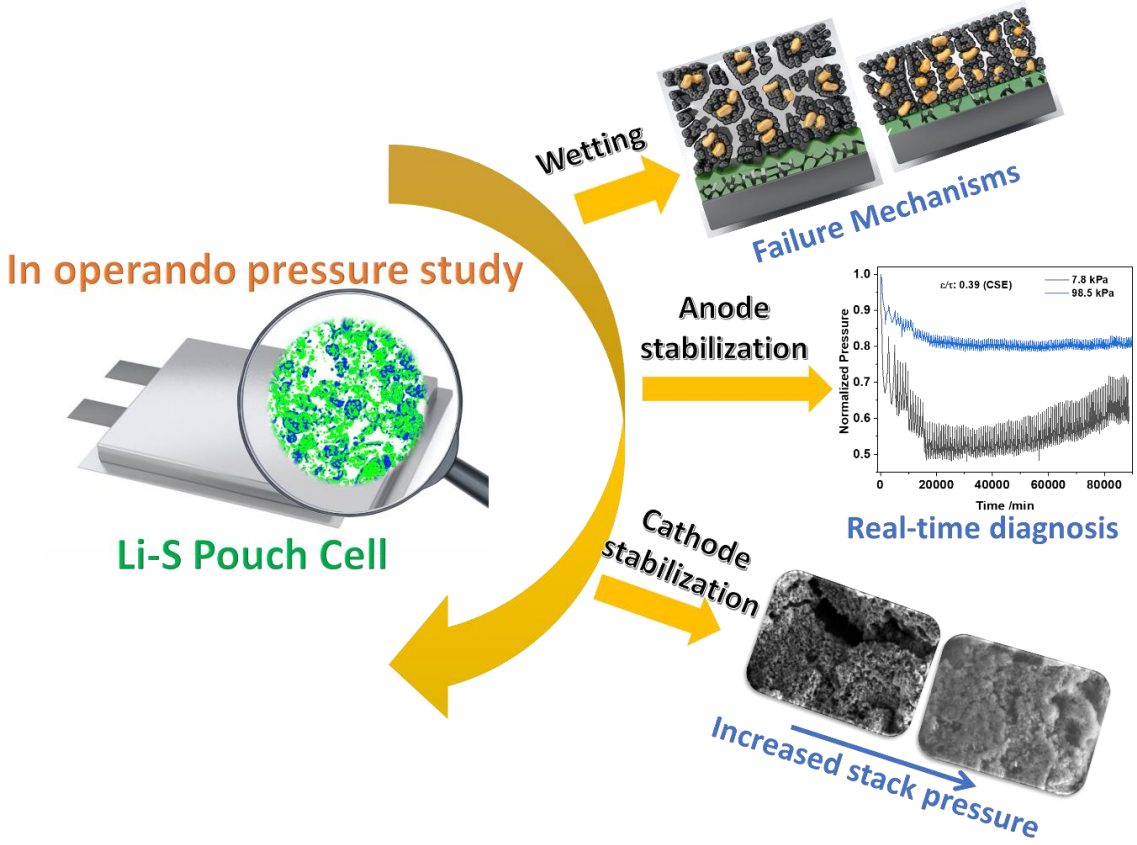

ToC

Supporting Information

Unlocking Failure Mechanisms and Improvement of Practical Li-S Pouch Cells Through in Operando Pressure Study

*Parameswara R. Chinnam[1], Leidong Xu[2], Lu Cai[3], Nikolaus L. Cordes[4], Sangwook Kim[1], Corey M. Efaw[1], Daniel J. Murray[5], Eric J. Dufek[1], Hongyi Xu[2] and Bin Li[1]**

[1]Energy Storage & Advanced Transportation Department, Idaho National Laboratory, Idaho Falls, ID 83415 US

[2]Mechanical Engineering, University of Connecticut, Storrs, CT 06269 US

[3]Materials Science and Engineering Department, Idaho National Laboratory, Idaho Falls, ID 83415 US

[4]Advanced Post Irradiation Examination Department, Idaho National Laboratory, Idaho Falls, ID 83415 US

[5]Advanced Characterization Department, Idaho National Laboratory, Idaho Falls, ID 83415 US

*E-mail: bin.li@inl.gov

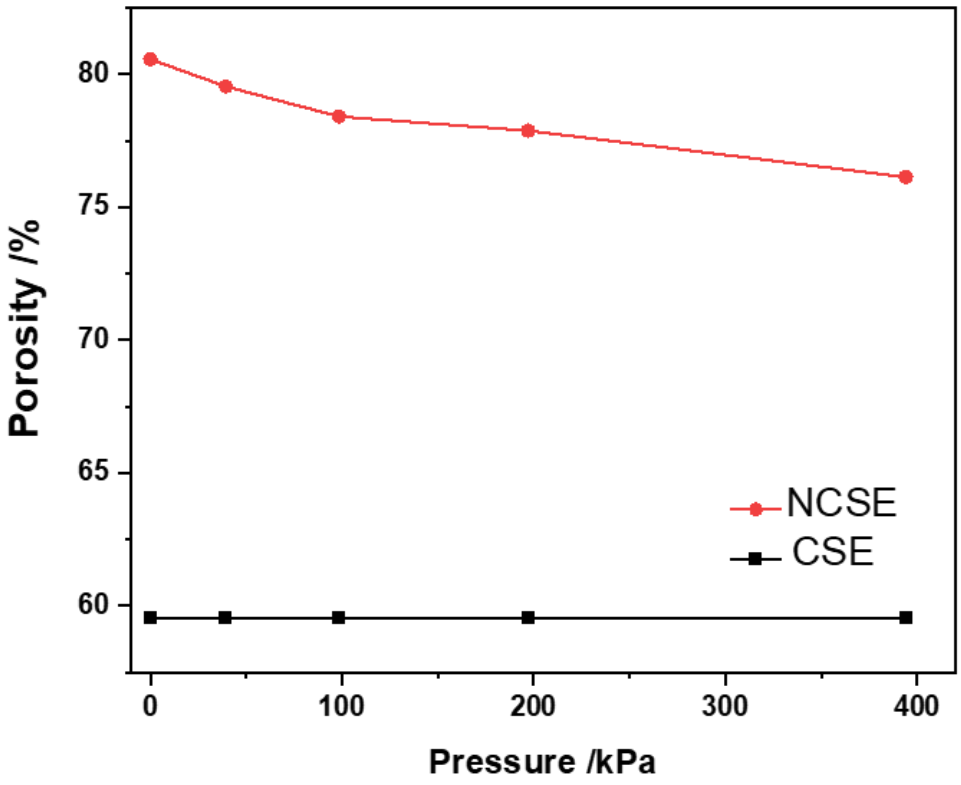

Figure S1 Comparison of porosity change of calendared and non-calendared sulfur electrodes with applied pressures.

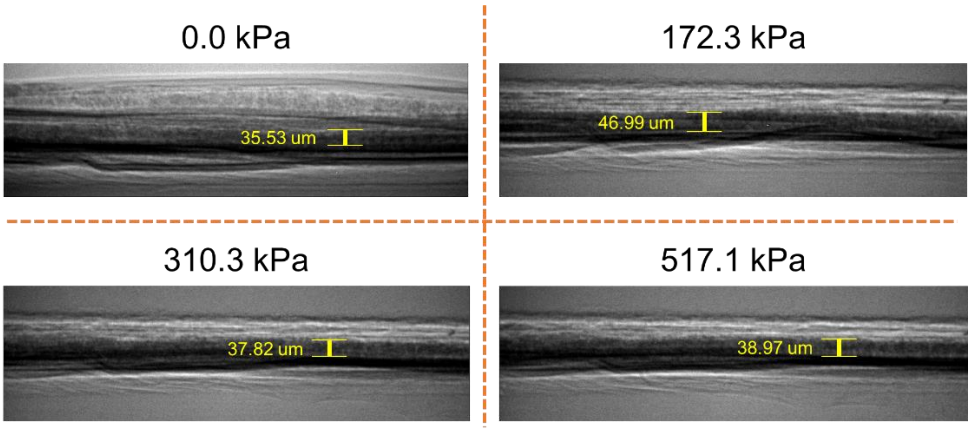

Figure S2 2D X-radiographs of CSE by in-situ applying different pressures.

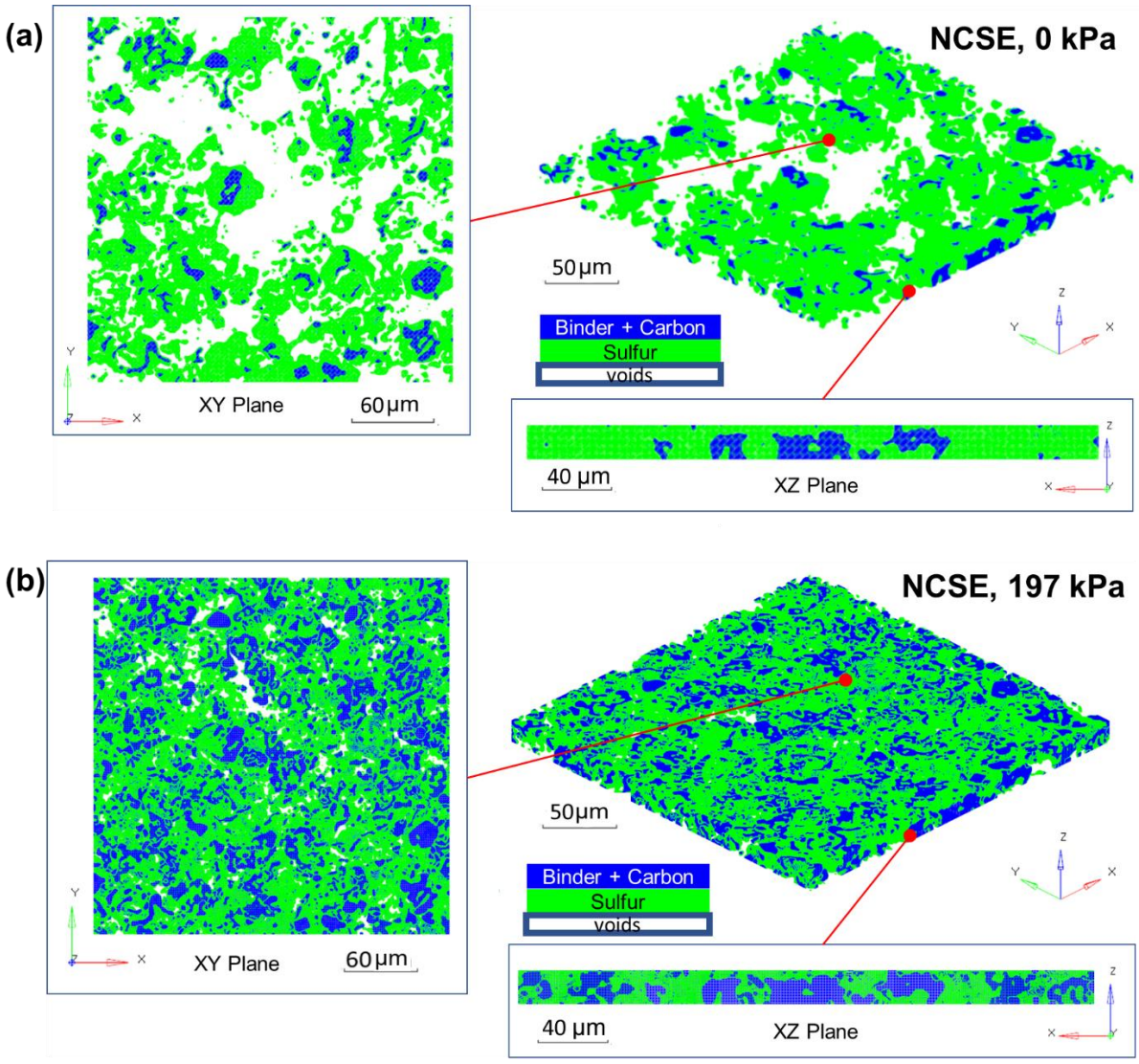

Figure S3 Micro-XCT images of 3D structures of NCSE without pressure(a) and under the pressure of 197 kPa (b).

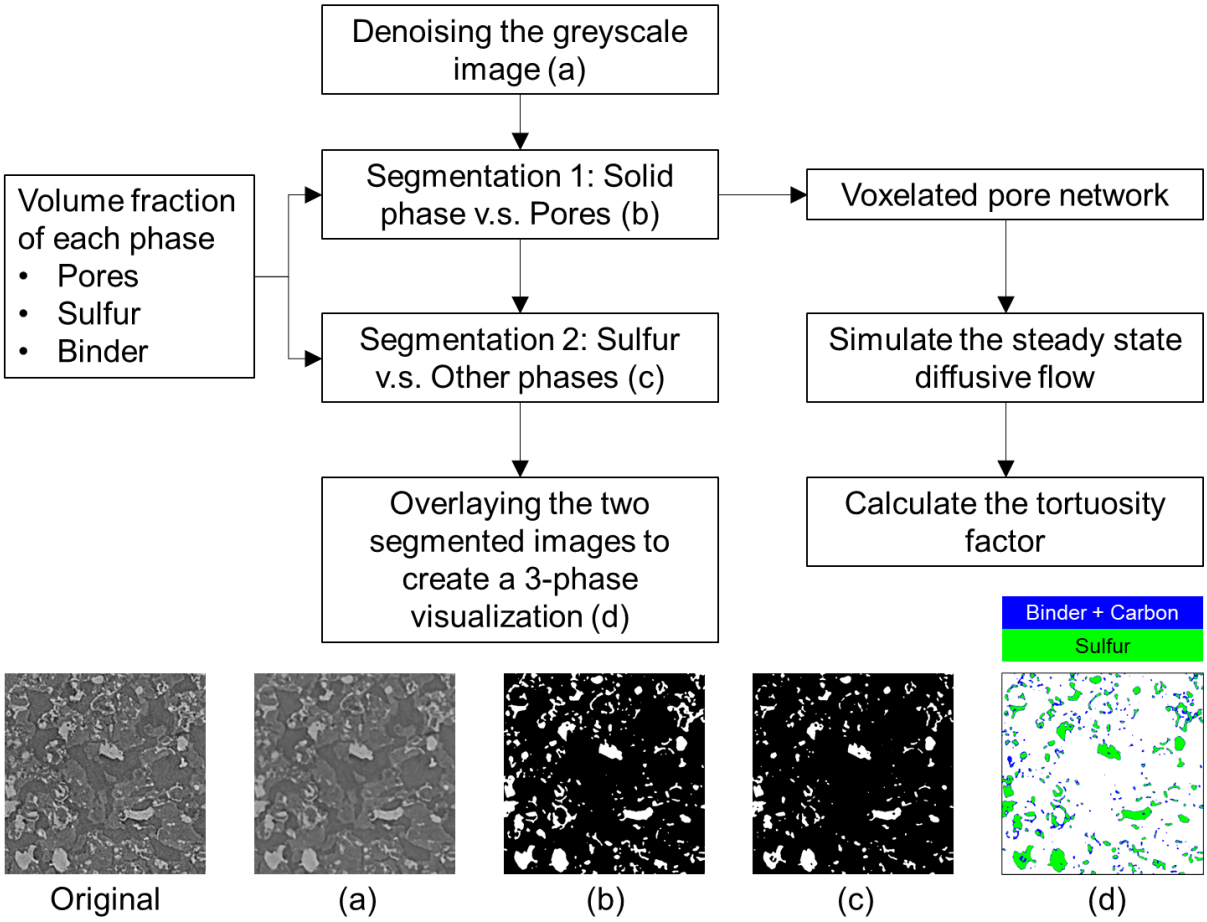

Figure S4. The microtructure-resolved modeling approach used in the calculation of tortuosity. (a) denoised greyscale 2D image from the reconstructed tomogram obtained via micro-XCT; (b) Binary image: white-solid phases, black-pores; (c) Binary image: white-sulfur, black-other phases; (d) 3-phase image: white-pores, blue-binder+carbon, green-sulfur.

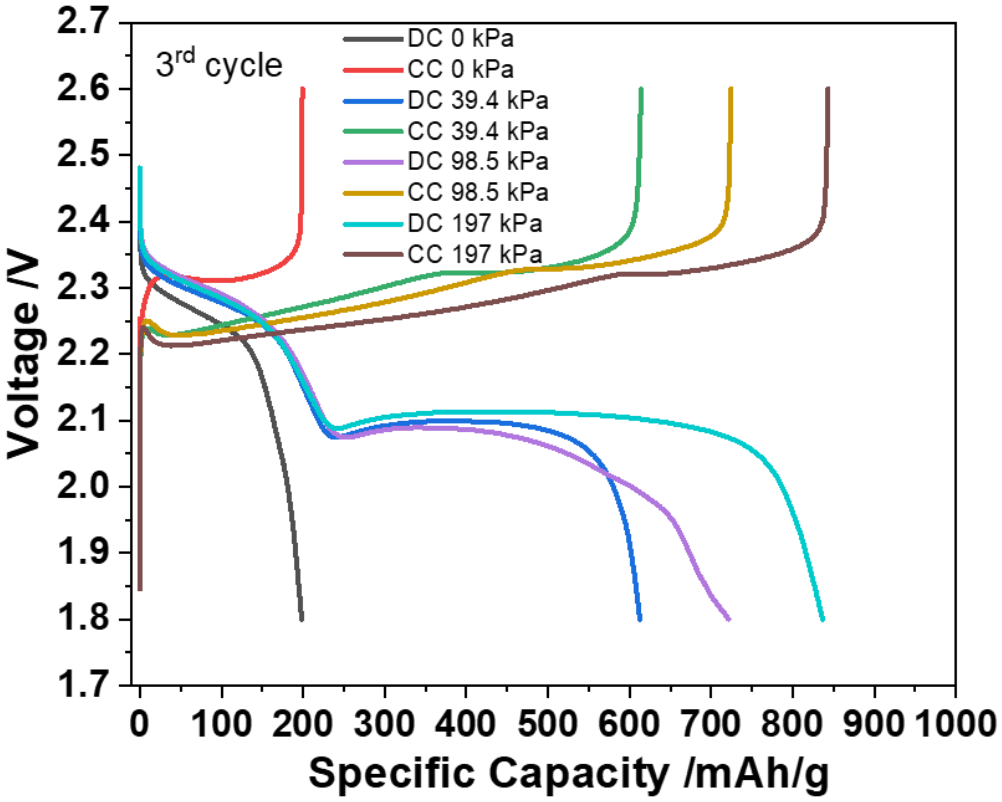

Figure S5. The plots of the charge capacities (CC) and discharge capacities (DC) vs. voltages of NCSE-based pouch cells under different pressures for the third cycle.

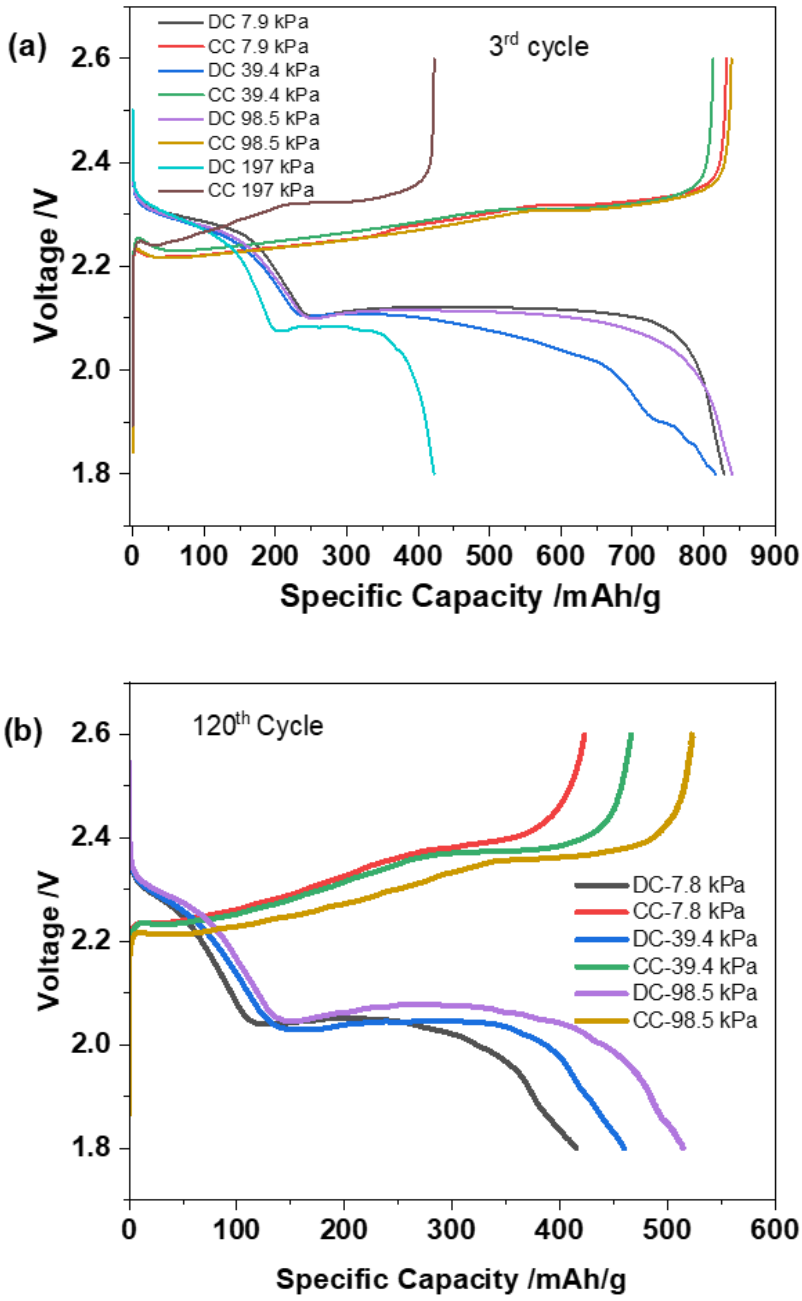

Figure S6. The plots of the charge capacities (CC) and discharge capacities (DC) vs. voltages of CSE-based pouch cells under different pressures for 3rd cycle (a) and 120th cycle (b).

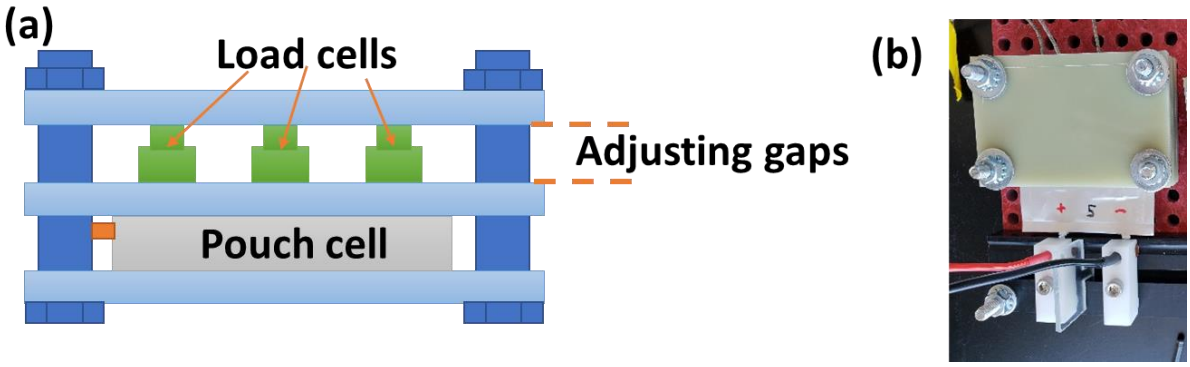

Figure S7. (a) Side view of schematic illustration of load cells in fixture (b) Picture of the experimental setup.

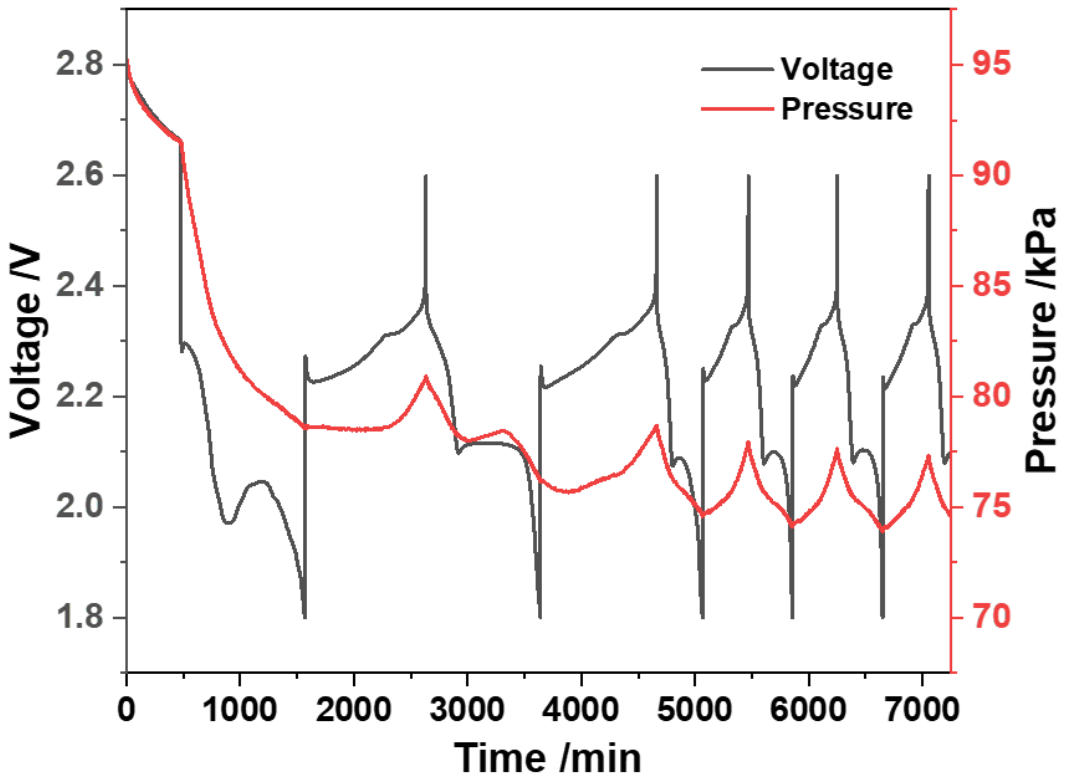

Figure S8. Voltage and pressure evolution of NCSE-based pouch cell under the pressure of 98.5 kPa during charge and discharge process.

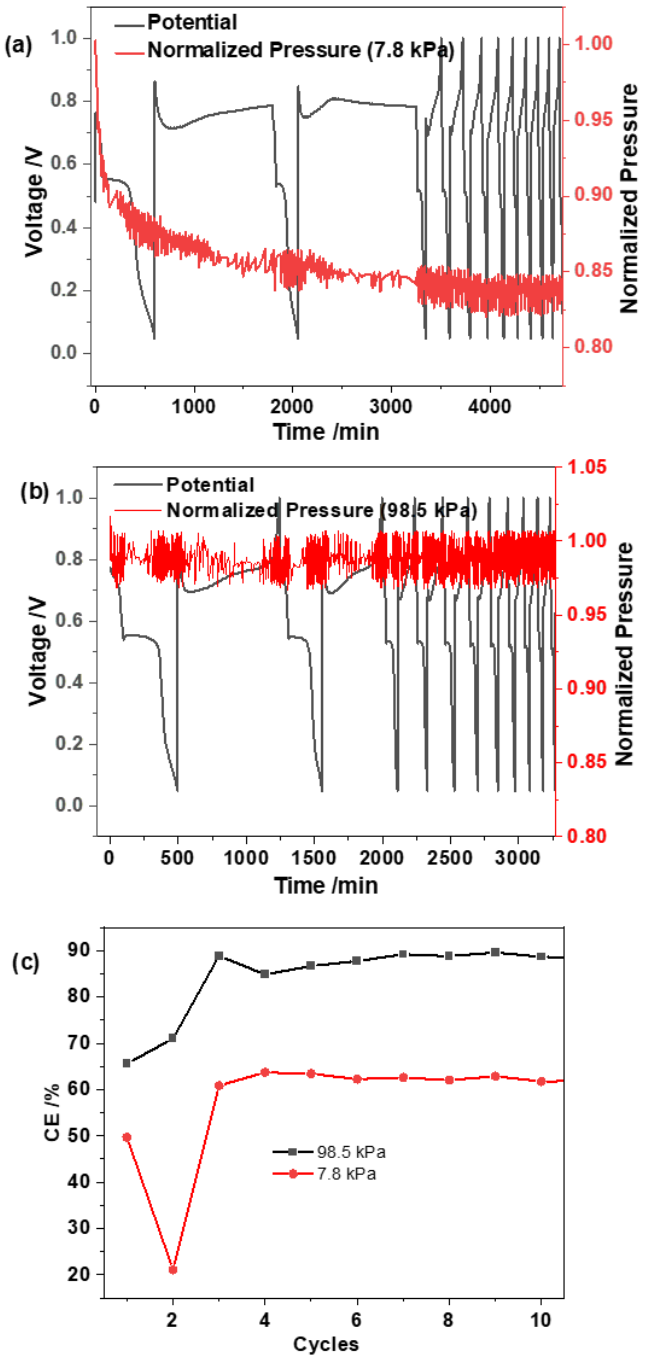

Figure S9 Voltage and pressure evolution of CSE-based lithiated LTO-S pouch cell under the pressures of 7.8 kPa (a) and 98.5 kPa (b) during charge and discharge process and their CE values over cycling (c).

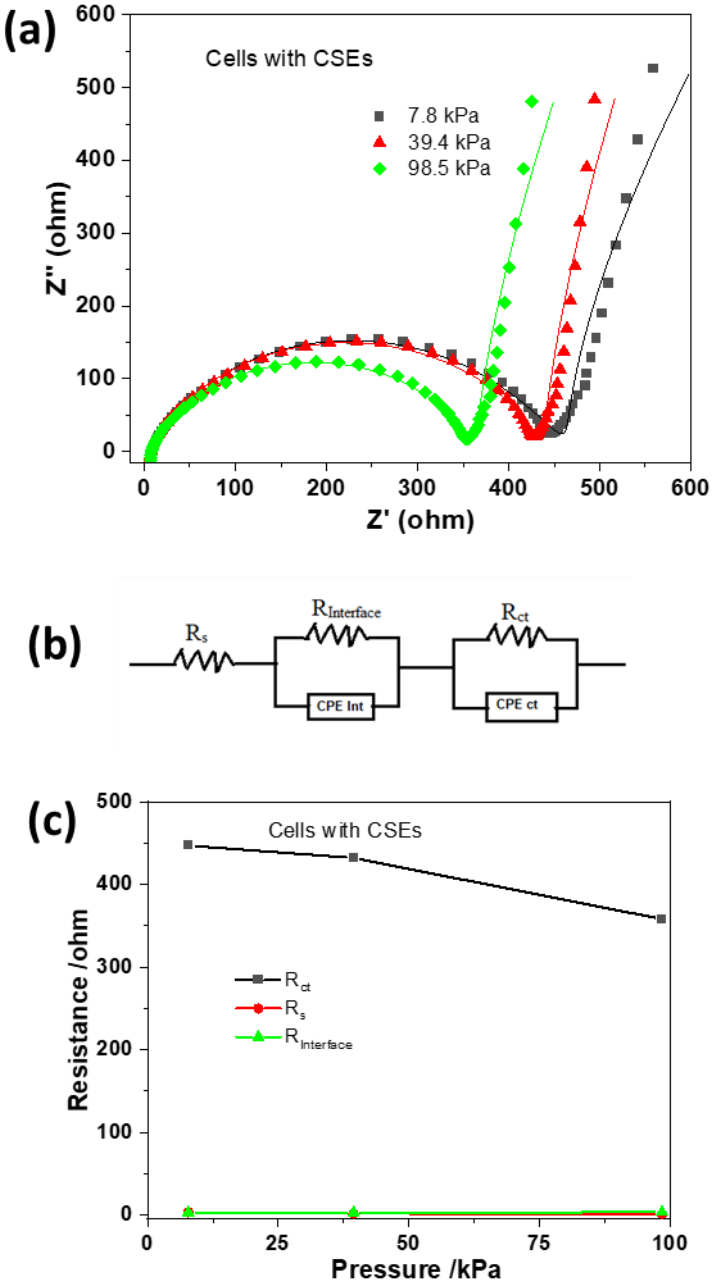

Figure S10 (a) Nyquist plots of CSE-based Li-S pouch cells under different pressures before running. Equivalent circuit (b) used for analysis of the Nyquist plots and fitted values are plotted in (c). R_s is bulk or solution resistance; $R_{Inferface}$ is interfacial resistance between Li metal anode and separator, separator and porous cathode; R_{CT} is the charge transfer resistance within the porous cathode.